ISIJ International, Vol. 60 (2020), No. 5, pp. 988–997

Characterisation of Binary Phase Mixtures of Magnesium-Aluminate Spinel and Calcium-Aluminates Using Time-Gated Raman Spectroscopy

Francis GYAKWAA,[1)]* Matti AULA,[1)] Tuomas ALATARVAS,[1)] Tero VUOLIO,[1)] Qifeng SHU,[1)] Marko HUTTULA[2)] and Timo FABRITIUS[1)]

1) Process Metallurgy Research Unit, University of Oulu, P.O. Box 4300, FI–90014, University of Oulu, Finland.
2) Nano and Molecular Systems Research Unit, University of Oulu, P.O. Box 4300, FI–90014, University of Oulu, Finland.

(*Received on September 6, 2019; accepted on November 5, 2019; J-STAGE Advance published date: January 9, 2020*)

The modification of $MgO{\cdot}Al_2O_3$ spinel inclusions into less detrimental mixture phases of CaO–MgO–Al_2O_3 plays an essential role in refining calcium-treated aluminium killed steels. This study uses Raman spectroscopy for the characterisation of binary phase samples that contain $MgO{\cdot}Al_2O_3$ spinel and calcium aluminate $(CaO)_x$–$(Al_2O_3)_y$ phases. Samples were synthesised from $MgO{\cdot}Al_2O_3$ spinel (MA), Al_2O_3 and calcium aluminate phases to achieve binary samples of CA–MA, C3A–MA, C12A7–MA and Al_2O_3–MA with varying phase fractions. The study also examined the possibility of a slight variation for non-stoichiometric spinel samples below the 1 600°C region in an MgO–Al_2O_3 binary system. The relative intensities of the Raman band were used for the quantification of the phase fractions. For a quantitative prediction, linear regression calibration models were identified for each of the studied systems. This work demonstrates the use of Raman spectroscopy for the characterisation of calcium aluminate phases of CA, C3A, C12A7 and magnesium aluminate spinel phases along with Al_2O_3 and its potential application in inclusion characterisation.

KEY WORDS: Raman spectroscopy; non-metallic inclusion; $MgO{\cdot}Al_2O_3$ spinel; calcium aluminate; characterisation.

1. Introduction

The production of high-quality steels with low amounts of inclusions is of great importance for both the producer and product user. In aluminium-killed steels, $MgO{\cdot}Al_2O_3$ spinel is an example of a potential inclusion that could be formed during the steelmaking process, and its existence could affect steel cleanliness.[1)] $MgO{\cdot}Al_2O_3$ spinel inclusions have some properties such as their high melting temperature, low deformability, irregular shape, which result in a high tendency to clog submerged entry nozzles in casting.[2,3)] These features can also be very harmful and could cause defects or fatigue fractures in the final products, significantly reducing the product quality.[2)] Depending on the form of interaction between liquid steel and the refractory[4,5)] or slag,[6)] the potential sources of MgO could be associated with the type of refractory materials used or with the slag composition. Many studies on spinel inclusions that concern their formation,[7,8)] and modification mechanisms[9–11)] have been conducted.

Calcium treatment has been reported[12,13)] to effectively modify the $MgO{\cdot}Al_2O_3$ spinel inclusions in Al-killed steels. The mechanism has been attributed to the formation of MgO–Al_2O_3–CaO inclusions, which could contain two or three phases. Additionally, the modification of spinel with calcium may lead to the formation of Al_2O_3–CaO–MgO inclusions that fall within the liquid region at steelmaking temperatures. Furthermore, the slag absorption process[14,15)] and other studies summarised by Park *et al.* (2010)[16)] demonstrate the development of control technologies for $MgO{\cdot}Al_2O_3$ spinel inclusions.

Various characterisation techniques[12,17–20)] for the quantification of $MgO{\cdot}Al_2O_3$ spinel and calcium aluminate inclusions have been studied. For example, the cathodoluminescence (CL) technique has been used to characterise both spinel[17)] and calcium aluminate inclusions.[18)] The use of Raman spectroscopy as an analytical technique makes it possible to obtain information such as the chemical composition and phase of the sample measured.[21–23)] Previous work[24–26)] has demonstrated that Raman spectroscopy techniques could be used for both the qualitative and quantitative characterisation of Raman active materials. However, the use of Raman spectroscopy as a characterisation technique for $MgO{\cdot}Al_2O_3$ spinel, and how this spinel associates with other oxide inclusions such as calcium aluminate have not been studied in much detail.

Although previous research work has used Raman spec-

* Corresponding author: E-mail: francis.gyakwaa@oulu.fi
DOI: https://doi.org/10.2355/isijinternational.ISIJINT-2019-576

troscopy to characterise spinel[27–32] and different calcium aluminate oxide phases,[33–36] the focus has mainly been on the characterisation of specific or individual phases. Additionally, Raman spectroscopy has also been used for characterising specific non-metallic inclusions.[37] However, mixtures containing both calcium aluminate and spinel phases have not been characterised or quantified in detail. Studies conducted on inclusions both on laboratory prepared and industrial steel samples demonstrate that inclusions mostly occur as a mixture of phases. Therefore, for Raman spectroscopy to be used as a potential characterisation technique for inclusion studies, further work on multiphase inclusion analysis relevant to steelmaking is required.

The purpose of this study is to demonstrate the application of Raman spectroscopy in the identification and characterisation of binary phase samples consisting of $MgO{\cdot}Al_2O_3$ spinel (MA), monocalcium aluminate, $CaO{\cdot}Al_2O_3$ (CA), mayenite $12CaO{\cdot}7Al_2O_3$ (C12A7), tricalcium aluminate, $3CaO{\cdot}Al_2O_3$ (C3A) and Al_2O_3. Additionally, this work will examine the effect of non-stoichiometric spinel on the Raman band (shift) position within a given range in the $MgO - Al_2O_3$ system measured with Raman spectroscopy.

2. Experimental

2.1. Preparation of Samples

Four sets of binary phase samples were prepared for this study. The binary phases included $CaO{\cdot}Al_2O_3$–$MgO{\cdot}Al_2O_3$(CA–MA), $3CaO{\cdot}Al_2O_3$–$MgO{\cdot}Al_2O_3$ (C3A–MA), $12CaO{\cdot}7Al_2O_3$–$MgO{\cdot}Al_2O_3$ (C12A7–MA) and Al_2O_3–$MgO{\cdot}Al_2O_3$ (A–MA). The spinel ($MgO.Al_2O_3$), monocalcium aluminate ($CaO{\cdot}Al_2O_3$) and aluminium oxide (Al_2O_3) were obtained from Alfa Aesar with a purity of approximately 99.9%. Calcium aluminate phase samples for C12A7 and C3A were prepared using calcium oxide (CaO) and aluminium oxide (Al_2O_3) powders obtained from Alfa Aesar (purity in the range of 99.7% to 99.9%) by varying the CaO/Al_2O_3 (C/A) ratio between 1.70 to 3.0 and sintered at a temperature of 1 350°C for 24 hours in a chamber furnace to achieve C12A7 and C3A phase samples.

A required proportion of MA, CA, C3A, C12A7 and Al_2O_3 were weighed for preparing the sample, then pressed into pellets, placed in crucibles and sintered in a chamber furnace. The samples were sintered at a temperature of 400°C for 24 hours to remove any moisture during the mixing process, which could potentially affect the subsequent analysis. This temperature was found suitable to prepare the samples since the phases remained unchanged based on the X-ray diffraction (XRD) analysis before and after this sintering process. The phase fraction of MA was varied between 10% and 90% for each binary phase sample (MA–CA, MA–C3A, MA–C12A7 and MA–Al_2O_3) prepared.

Samples of a non-stoichiometric spinel range within the $MgO–Al_2O_3$ binary system were prepared by adding of an excess amount (2, 5 and 10 wt-%) of magnesia (MgO) and alumina (Al_2O_3) to the reference spinel (obtained from Alfa Aesar, with a purity of 99.9%), and sintered in the chamber furnace at a high temperature of 1 600°C for 24 hours. The pellets were milled into a powder, characterised by XRD X-ray fluorescence (XRF) and followed with a Raman spectroscopy measurement.

2.2. Characterisation of the Samples

The prepared samples were identified, and the weight percent of the phases was estimated using XRD. The XRD set-up consisted of Bragg-Brentano para-focusing geometry (300 mm goniometer) with an acquisition speed of 3 degrees per minute with 0.02 degrees per step. It had a Cu source lamp with 45 kV and 200 mA settings with a 9-kW rotating anode and used a 10 mm length limiting slit for the source side of the samples in standard glass holders with 5 degree Soller slits used on both sources, and the analyser side. Further verification of the samples' chemical composition was evaluated by conducting an elemental analysis with the use of XRF. The XRF instrument used was an Axios Max model from Panalytical which consisted of an X-ray generator Rh tube, a maximum power of 4 kW and with SuperQ as its analysis software.

2.3. Raman Spectroscopy

Raman spectroscopy as an analytical technique uses an inelastic scattering of monochromatic light to cause a change in the bond, which is a characteristic function of the vibrational modes of the molecules in the material.[21,23] Based on the interaction between the laser beam and the molecular vibration in the sample, it is possible to identify a specific composition from the Raman spectrum measured as a fingerprint of the individual component present in the sample. **Figure 1** shows a schematic diagram that indicates the information that can be obtained from a Raman spectrum from a sample measured with Raman spectroscopy.[21–23] The a) intensity (I) indicates the component concentration in the material, b) band (shift) position shows the structure, phase or stoichiometric content, c) the full width at half maximum (FWHM) illustrates the crystallinity, doping or the defects of the sample and band (shift) direction attributable to the effect of stress, pressure and temperature.

The Raman spectroscopy measurements were carried out in ambient conditions by using a TimeGated® Raman spectrometer (TG532 M1) obtained from TimeGated instruments Ltd., Finland. The spectrometer was equipped with a pulsed laser of 532 nm, fibre-coupled, with a shot length of 150 ps and a frequency range from 40 to 100 kHz. The laser had a spectral width of less than 0.1 nm, and a power range from 30 to 60 mW. The probe head was made of 200 μm collection fibre with a spot size of 1 mm, with Photonics RPB532 w/105 μm excitation fibre. The TG532 M1 spec-

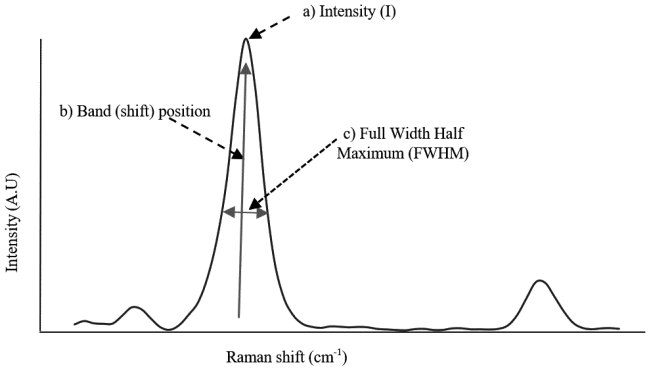

Fig. 1. An example of a Raman spectrum and corresponding measured material information.

trometer component also included a CMOS-SPAD array detector, a fibre-coupled spectrograph, and delay electronics. The spectra acquisition time of 3–5 minutes and Raman spectra range of 100–1 200 cm^{-1} with a resolution of 10 cm^{-1} were used in this work for the sample measurements. The samples were measured several times, and a good reproducibility was observed between the Raman spectra acquired. A rotating sample holder stage was used during the measurement to obtain the average spectra.

2.4. Calibration Model

The relation between different Raman peak ratios and the phase content in the samples were analysed using a calibration model. The variance in the phase content in the sample was estimated by using the summed Raman spectrum to define the relative intensities of the peaks present in the Raman spectrum. The calibration candidate was given by:

$$x_c = \frac{I_k}{(I_n + I_k)}, \quad \ldots\ldots (1)$$

where x_c is the calibration feature candidate, I_k is the intensity for the Raman shift k, and I_n is the intensity corresponding to the Raman shift n. The evaluation of the model performance for each of the calibration feature candidates was carried out using a leave-multiple-out cross-validation procedure.[38,39] For cross-validation, the data was split so that 20% was used for validation and 80% for training. The calibration parameters were identified using the method of least-squares. The model performance and distribution of the calibration parameters were assessed by repeating the cross-validation 4N times. The final selection was carried out choosing the relative intensity and a model parameter distribution that minimised the average mean absolute error for the training and validation sets for 4N repetitions. The stability of the calibration feature candidates were evaluated by calculating the ratio of the mean and the standard deviation for a standardised regression coefficient, as well as the mean absolute error for training and validation sets for 4N repetitions. A more detailed description of this procedure is presented in our earlier work.[40]

3. Results and Discussion

3.1. Characterisation and Phase Analysis

The sample phase identification was conducted using XRD, as illustrated in **Figs. 2**–**4**, that show an example of the XRD spectra for some selected samples for CA–MA (Fig. 2), C12A7–MA (Fig. 3) and C3A–MA (Fig. 4), where *i, ii* and *iii* correspond to 20%, 60% and 80% phase fractions of MA in each sample. The elemental composition for the samples was analysed with XRF.

Both XRF and XRD were used to verify the sample composition since these measurement techniques provide different information about the same sample measured. XRF gives the weight percentage of the identified elements while XRD measures the intensity of the crystal diffraction peaks due to the individual chemical compounds and for phase identification in the sample. Therefore, the two serve as complementary techniques to assist in verifying the initial sample composition.

Tables 1 and **2** show the phase weight percentages for

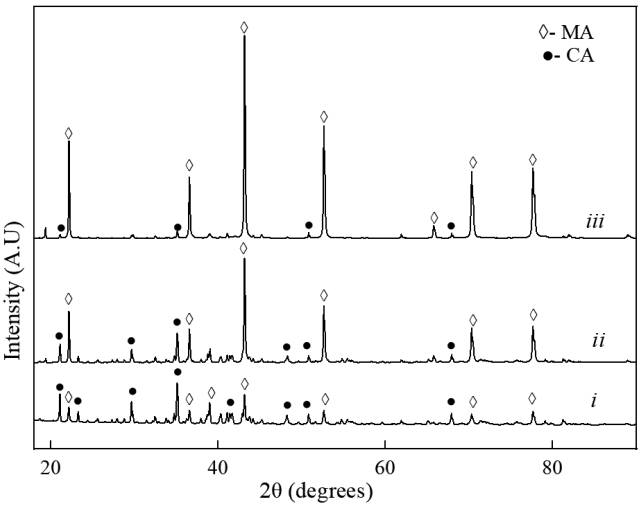

Fig. 2. XRD spectra for binary samples of MA and CA: i) 20% of MA, ii) 60% of MA and iii) 80% of the MA phase component.

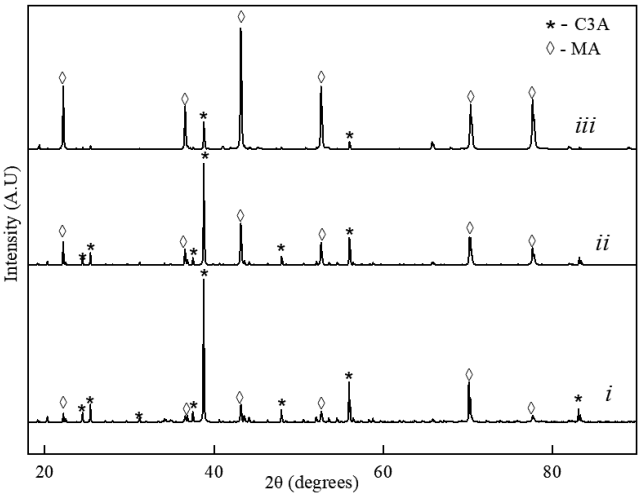

Fig. 3. XRD spectra for a binary sample of MA and C3A: i) 20% of MA, ii) 60% of MA and iii) 80% of the MA phase component.

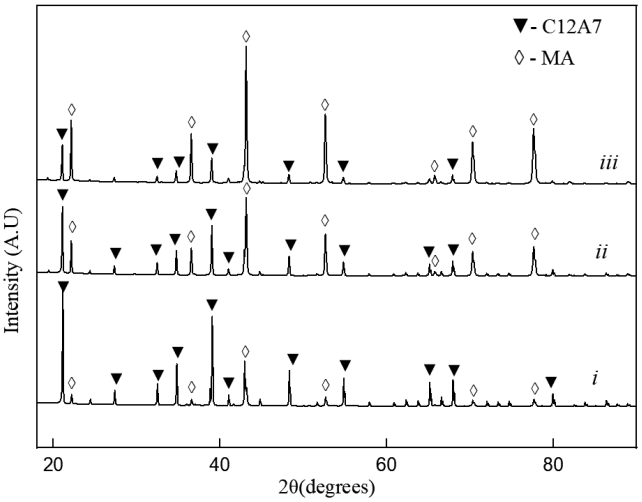

Fig. 4. XRD spectra for a binary sample of MA and C12A7: i) 20% of MA, ii) 60% of MA and iii) 80% of the MA phase component.

Table 1. Initial sample composition and XRF analyses for binary aluminates spinel-calcium aluminates phases of C12A7–MA and CA–MA.

	Initial phase composition (wt%)		XRF results and calculated phase composition (wt%)					Initial phase composition (wt%)		XRF results and calculated phase composition (wt%)				
	C12A7	MA	Ca	Al	Mg	C12A7	MA	CA	MA	Ca	Al	Mg	CA	MA
1	85	15	32.4	26.4	2.9	85	15	90	10	26.7	31.8	1.5	87	13
2	81	19	31.2	26.8	3.5	82	18	80	20	23.6	33.4	2.3	79	21
3	76	24	29.8	27.8	3.4	81	19	70	30	20.6	33.7	4.5	68	32
4	67	34	24.1	29.3	6.6	64	36	60	40	18.2	34.5	5.6	55	45
5	43	57	17.5	32.5	8.5	50	50	50	50	15.4	35.3	7.0	45	55
6	38	62	15.3	33.2	9.6	44	56	40	60	13.0	36.9	7.3	37	63
7	29	72	9.6	35.2	12.1	28	72	30	70	10.3	36.8	9.7	29	71
8	19	81	8.0	36.3	12.2	24	76	20	80	7.6	37.8	10.8	21	79
9	10	90	4.5	37.8	13.4	13	87	10	90	4.6	38.9	12.1	13	87
10	5	95	2.4	39.0	13.8	7	93	5	95	2.5	39.3	13.3	7	93

Table 2. Initial sample composition and XRF analyses for binary aluminates spinel, calcium aluminates phase and Al_2O_3 of C3A–MA and A–MA.

	Initial phase composition (wt%)		XRF results and calculated phasecomposition (wt%)					Initial phase composition (wt%)		XRF results and calculated phase composition (wt%)			
	C3A	MA	Ca	Al	Mg	C3A	MA	A	MA	Al	Mg	A	MA
1	88	12	43.2	18.9	2.3	88	12	85	15	51.6	1.5	86	14
2	78	22	39.4	21.0	3.1	83	17	70	30	50.7	2.6	73	27
3	69	31	32.7	23.0	6.5	66	34	60	40	49.8	3.6	64	36
4	59	41	31.3	24.7	5.8	52	48	55	45	49.4	4.0	60	40
5	54	46	23.0	28.8	8.1	47	53	50	50	49.0	4.5	55	45
6	49	51	22.1	28.0	9.7	43	57	45	55	48.5	5.0	50	50
7	39	61	19.4	30.0	9.7	26	74	40	60	47.9	5.7	46	54
8	29	71	12.8	32.8	12.2	20	80	30	70	47.4	6.3	37	63
9	10	90	5.3	37.2	13.4	12	88	20	80	44.8	9.3	25	75
10	5	95	3.6	38.4	13.4	7	93	10	90	42.7	11.6	13	87

the initial composition for the samples prepared and the XRF phases estimated based on elemental analysis. The XRF results were normalised to phase compositions to enable easier comparison to XRD assuming stoichiometric phases and that the samples contained only XRD analysed phases. **Table 3** shows the measurements carried out with XRF for the non-stoichiometry spinel samples and this was also evaluated by assuming an unlimited supply of oxygen to achieve the oxide compounds (Al_2O_3 and MgO) for the excess amount of Al_2O_3 and MgO added to reference spinel samples.

Table 3. Excess amount of Al_2O_3 and MgO added to reference spinel samples and XRF analyses.

Initial sample addition		XRF analysis (wt%)	
	wt%	MgO	Al_2O_3
MA		24.6	75.4
Al_2O_3	2	24.2	75.8
	5	23.3	76.7
	10	22.0	78.0
MgO	2	26.7	73.3
	5	27.6	72.4
	10	39.4	60.6

Table 4 shows the main Raman shift (peaks) identified for each phase in the samples measured and the published reference Raman shift. The Raman shifts (cm^{-1}) identified for the specified phases in this study agree with previous studies within a Raman shift range of $\pm$ 5 cm^{-1}.

Figures 5–8 show a change in Raman peak intensities and these figures illustrate some examples of the binary phase Raman spectra. As explained in section 2.3, the phase fraction in the sample measured can be determined by observing the change in the relative Raman intensity of the peaks. Therefore, the evaluation of relative intensity could be used to estimate the content of a specific phase present in a sample.

Figure 5 shows the spectra for samples that contain C12A7 and magnesium aluminate spinel (MA), which

Table 4. Reference and measured Raman shift (cm^{-1}) for calcium aluminate and spinel phases. (where s is strong, m is medium, and w is weak).

Phase	Measured peaks [Raman shift (cm^{-1})]	Reference [Raman shift (cm^{-1})]
Al_2O_3	422 *s*, 380 *m*, 583 *m*, 648 *m*, 752 *m*	413 – 420[41,42] *s*, 375 – 380[41,42] *m*, 642 – 648[41,42] *m*, 748 – 750[41,42] *m*, 573 – 579[41,42] *m*
CA	522 *s*, 549 *m*, 790 *w*	520 – 521[33,34,36] *s*, 545 – 547[33,34,36] *m*, 790 – 793[33,34,36] *w*
C12A7	517 *s*, 781 *m*, 314 *m*	312 – 333[35,36] *m*, 516 – 517[35,36] *m*, 772[35,36] *m*, 779[35,36] *m*
C3A	756 *s*, 508 *m*,	756 –757[34,36] *s*, 140 –150[34,36] *w*, 506 –508[34,36] *m*
$MgO.Al_2O_3$	416 *s*, 674 *m*, 773 *m*	409 – 412[27–32] *s*, 767 – 772[27–32] *m*, 666 – 674[27–32] *m*, 312– 313[27–32] *m*

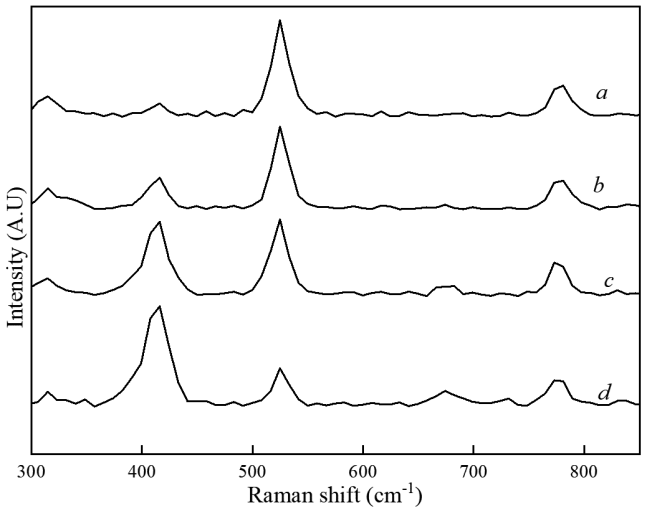

Fig. 5. Raman spectra for a binary C12A7–MA phase sample: MA content a) 20 wt%, b) 40 wt%, c) 60 wt% and d) 80 wt%.

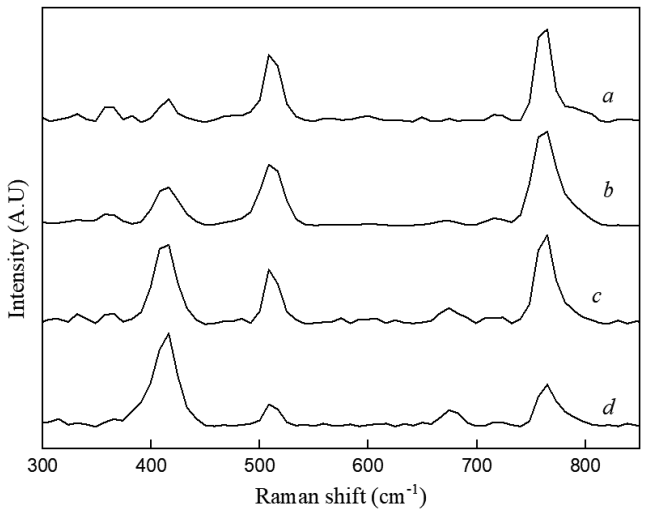

Fig. 6. Raman spectra for a binary C3A–MA phase sample; MA content a) 20 wt%, b) 40 wt%, c) 60 wt% and d) 80 wt%.

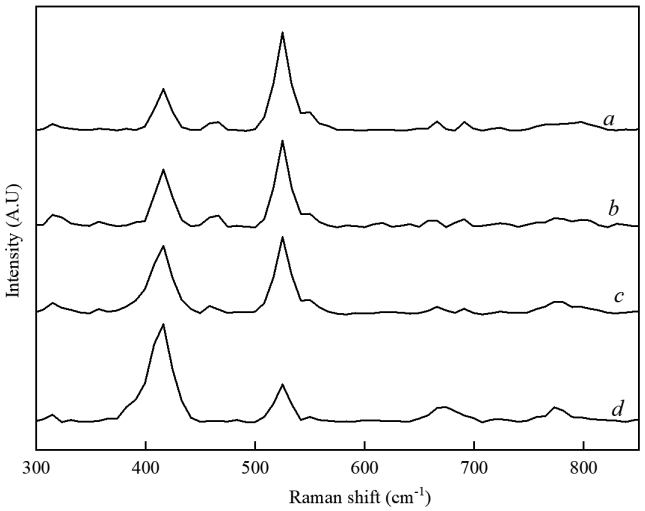

Fig. 7. Raman spectra for a binary CA–MA phase sample; MA content a) 20 wt%, b) 40 wt%, c) 60 wt% and d) 80 wt%.

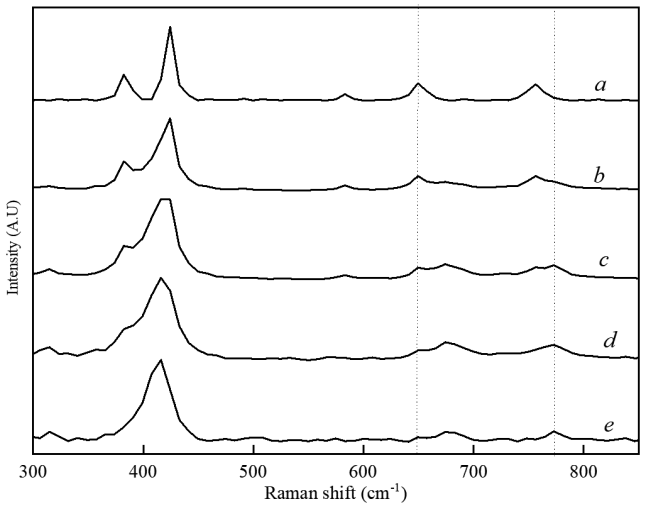

Fig. 8. Raman spectra for the binary A–MA phase sample; MA content a) 0 wt%, b) 20 wt%, c) 40 wt% and d) 60 wt% and 80 wt%.

illustrates that an increment in the MA phase fraction in the sample had a corresponding increase in the Raman shift region of 410–420 cm^{-1}. This rise in intensity could be attributed to the increasing content of MA since the most intense peak for this phase is located around 416 cm^{-1}. A corresponding increase in the Raman shift in the region of 517–520 cm^{-1} was noticed when the phase fraction for C12A7 was increased since the most intense Raman shift was located at 517 cm^{-1} for C12A7.

For Raman spectra measured from samples comprising of C3A and MA, it was also observed that the peak intensity within the Raman shift region of 410–420 cm^{-1} rose when the phase content of MA in the C3A–MA sample was increased. The peak within the Raman shift region of 756–765 cm^{-1} also increased when the phase fraction of C3A in the sample rose. These phenomena could be observed in Fig. 6 for C3A–MA samples where the most intense peak for MA is at 416 cm^{-1} and for C3A it is at 756 cm^{-1}.

Figure 7 shows the Raman spectra obtained from samples that contain CA and MA, where it was noticed that when CA content was increased, the Raman spectra showed a rise in the peak intensity in the region of 520–524 cm^{-1}. A peak shoulder in the 545–549 cm^{-1} region was observed, which is a characteristic feature for the CA phase as the phase content increases. A similar trend could also be noted when the phase content for MA increased, the peak intensity in the Raman shift region of 416–420 cm^{-1} also increased. This is associated with MA because the most intense peak is located around 416 cm^{-1}.

In Fig. 8, the Raman spectra show samples containing only Al_2O_3 and MA. The most intense peaks for Al_2O_3 and MA in the Al_2O_3–MA samples could not directly be used to distinguish the changes in the phase content because of peak overlap. However, the medium peaks could be used to observe the difference in the phase content, where an increase in Al_2O_3 content showed a gradual rise in the Raman peak around 380 cm^{-1}. Additionally, an increase in the MA content in the sample demonstrates the appearance of medium peaks at 674 and 772 cm^{-1}, which are attributable to MA.

3.2. Calibration Model Selection

The estimation of the phases present in the samples was carried out using linear calibration models that established the relation between the relative intensities of the Raman band and phase fractions. The calibration model and stability of the calibration variable candidates and the stability estimation and construction are presented in section 2.4. The calibration models, as explained in section 2.4, were built based by making use of the phase content based on an XRF evaluation and the phases identified with XRD as the dependent variable.

Tables 5–**8** show the estimated average values of the coefficient of determination and mean absolute error for 4*N* data splits. **Figures 9**, **11**, **13** and **15** show the relative stabilities of the calibration variable candidates and with the mean absolute error values (MAE) for the training and validation sets. The most stable calibration variable candidate was estimated to be the one with the highest degree of repeatability and accuracy resulting from a small deviation of the normalised calibration parameters between the repetitions.

3.2.1. C12A7–MA Samples

Based on the analysis, for samples that contain C12A7 and MA, Table 5 shows that the most suitable peak intensity ratio with the best coefficient of determination values and the lowest mean absolute error (MAE) is 517 cm^{-1} for C12A7 and 416 cm^{-1} for MA for both training and validation sets. The suggested peaks are also seen as the most intense ones in the Raman spectrum. Figure 9 demonstrates that the Raman shift ratio 517/416 is more stable than the other peaks, which indicates a low noise and thus

Table 5. Estimation of the coefficient of determination (R^2) and mean absolute error (MAE) of the prediction and validation between the relative intensity of the peaks and phase content based on XRF for C12A7–MA.

Phases	Relative intensity	Training data		Validation		Relative Stability
		Mean (R^2)	Mean (MAE)	Mean (R^2)	Mean (MAE)	
C12A7–MA	517/416	0.99	0.08	0.99	0.08	0.71
C12A7–MA	517/674	0.86	0.31	0.87	0.32	0.05
C12A7–MA	781/416	0.96	0.17	0.96	0.18	0.18
C12A7–MA	781/674	0.91	0.25	0.91	0.26	0.06

Table 6. Estimation of the coefficient of determination (R^2) and mean absolute error (MAE) of the prediction and validation between the relative intensity of the peaks and phase content based on XRF for C3A–MA.

Phases	Relative intensity	Training data		Validation (ExVal)		Relative Stability
		Mean (R^2)	Mean (MAE)	Mean (R^2)	Mean (MAE)	
C3A–MA	756/416	0.98	0.13	0.98	0.15	0.52
C3A–MA	508/416	0.97	0.13	0.97	0.14	0.40
C3A–MA	756/674	0.72	0.44	0.77	0.49	0.04
C3A–MA	508/674	0.67	0.47	0.78	0.54	0.03

Table 7. Estimation of the coefficient of determination (R^2) and mean absolute error (MAE) of the prediction and validation between the relative intensity of the peaks and phase content based on XRF for CA–MA.

Phases	Relative intensity	Training data		Validation (ExVal)		Relative Stability
		Mean (R^2)	Mean (MAE)	Mean (R^2)	Mean (MAE)	
CA–MA	522/416	0.97	0.13	0.97	0.15	0.60
CA–MA	549/416	0.92	0.21	0.92	0.23	0.20
CA–MA	522/674	0.73	0.44	0.77	0.47	0.09
CA–MA	549/674	0.85	0.28	0.85	0.29	0.10

Table 8. Estimation of the coefficient of determination (R^2) and mean absolute error (MAE) of the prediction and validation between the relative intensity of the peaks and measured phase content based on XRF for A–MA.

Phases	Relative intensity	Training data		Validation (ExVal)		Relative Stability
		Mean (R^2)	Mean (MAE)	Mean (R^2)	Mean (MAE)	
A–MA	648/682	0.93	0.22	0.95	0.26	0.10
A–MA	648/773	0.94	0.19	0.96	0.21	0.16
A–MA	648/416	0.88	0.28	0.92	0.38	0.07
A–MA	648/674	0.93	0.22	0.95	0.25	0.11
A–MA	380/773	0.90	0.25	0.91	0.29	0.08
A–MA	380/682	0.91	0.24	0.91	0.30	0.06
A–MA	380/416	0.90	0.26	0.92	0.33	0.06
A–MA	380/674	0.91	0.23	0.93	0.28	0.07
A–MA	422/773	0.90	0.25	0.91	0.28	0.07
A–MA	422/682	0.91	0.24	0.92	0.26	0.06
A–MA	422/416	0.92	0.24	0.92	0.27	0.08
A–MA	422/674	0.93	0.21	0.93	0.25	0.08

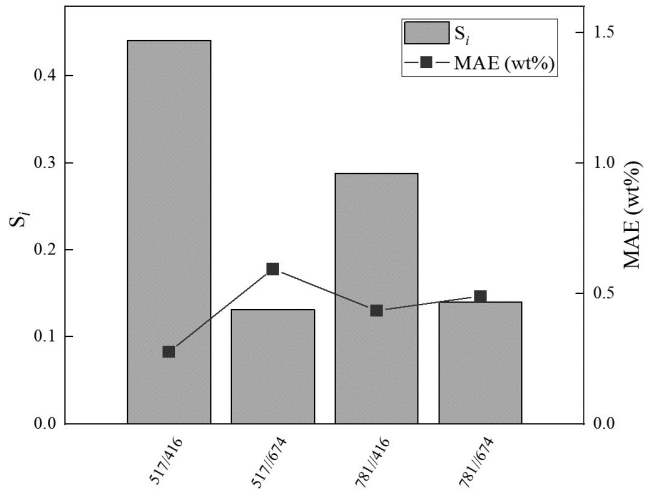

Fig. 9. Estimation for relative stabilities (S_i) of the calibration variable candidates and mean absolute error values for training and validation sets for C12A7–MA.

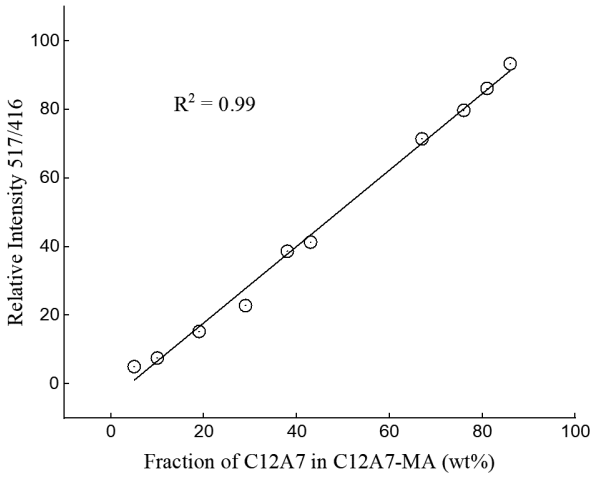

Fig. 10. Raman spectroscopy estimation for the phase content (wt%) for C12A7 as a function of the phase content of C12A7 in a spinel-calcium aluminate binary phase sample (C12A7–MA).

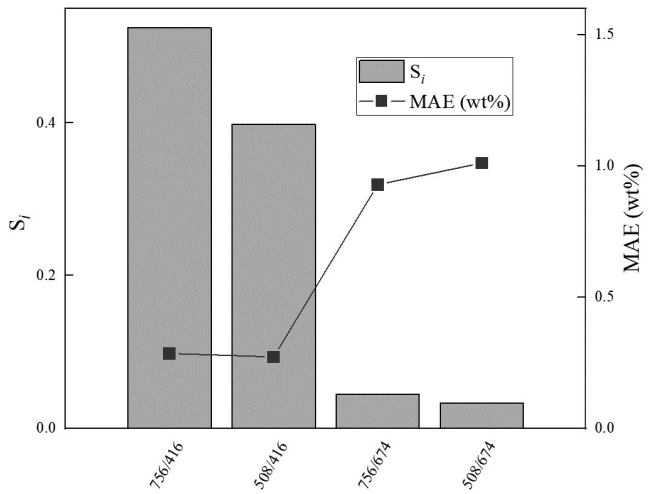

Fig. 11. Estimation for relative stabilities (S_i) of the calibration variable candidates and mean absolute error values for training and validation sets for C3A–MA.

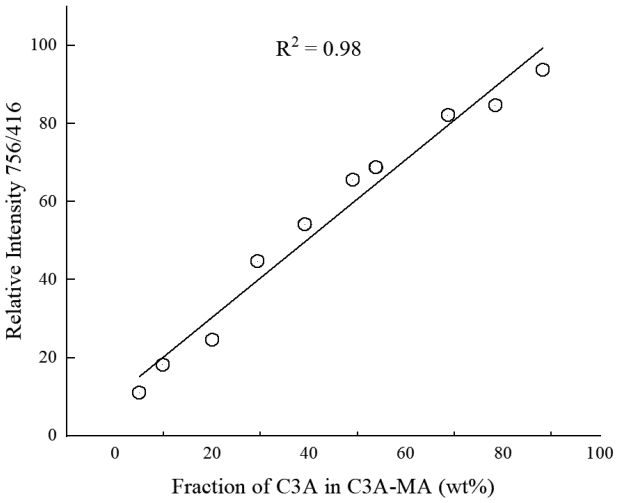

Fig. 12. Raman spectroscopy estimation for the phase content (wt%) for C3A as a function of the phase content of C3A in a calcium aluminate-spinel binary phase (C3A–MA).

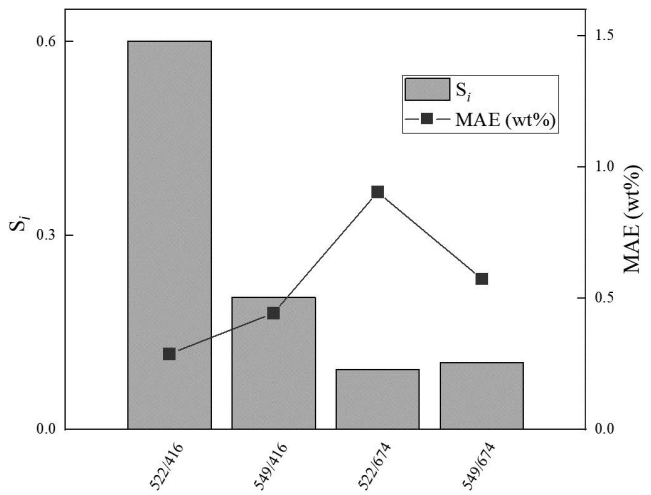

Fig. 13. Estimation for relative stabilities (S_i) of the calibration variable candidates and mean absolute error values for training and validation sets for CA–MA.

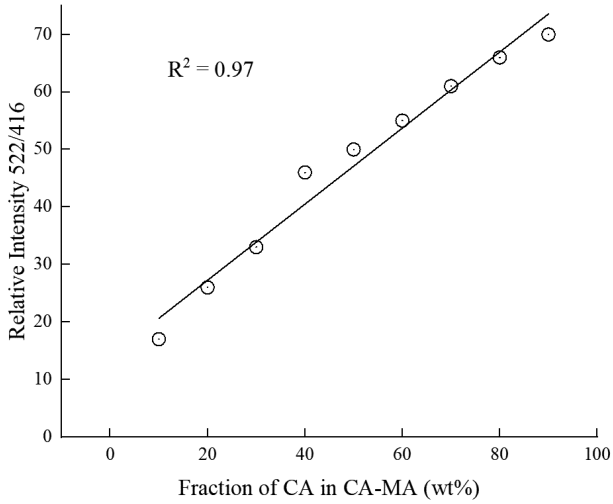

Fig. 14. Raman spectroscopy estimation for the phase content (wt%) for CA as a function of the phase content of CA in a calcium aluminate – spinel binary phase (MA–CA).

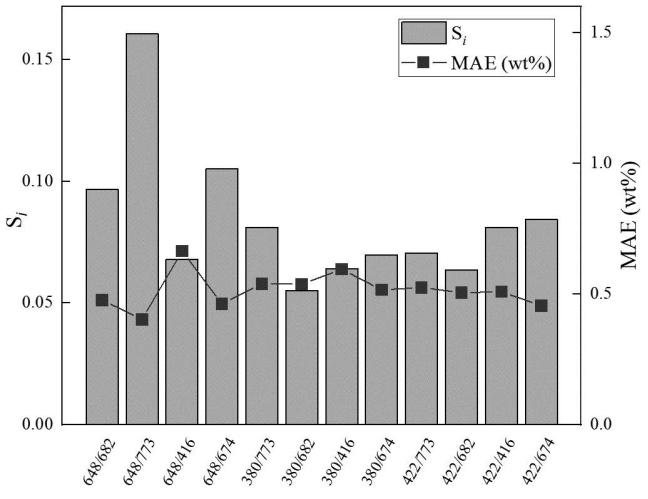

Fig. 15. Estimation for relative stabilities (S_i) of the calibration variable candidates and mean absolute error values for training and validation sets for CA–MA.

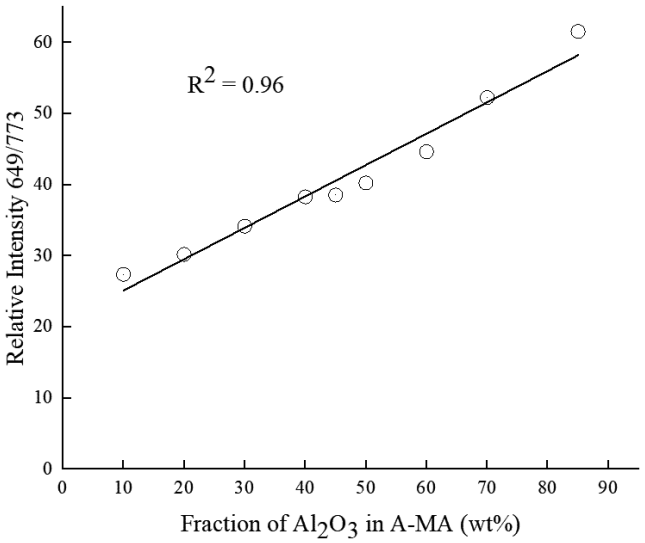

Fig. 16. Raman spectroscopy estimation for the phase content (wt%) for A as a function of the phase content of Al_2O_3 in an aluminium oxide – spinel binary phase (A–MA).

low scatter in the data. **Figure 10** represents the relative intensities as a function of the phase fraction. Therefore, for the $MgO{\cdot}Al_2O_3$–$12CaO{\cdot}7Al_2O_3$ (C12A7–MA) samples, the relative intensity ratio of 517/416 was the best indicator for changes in C12A7/MA ratio.

3.2.2. C3A–MA Samples

For samples of C3A–MA, it can be observed in Table 6 that the ratio of the intensities of Raman shifts at 756 cm^{-1} for C3A and 416 cm^{-1} for MA had the lowest mean absolute error (MAE) with the best coefficient of determination (R^2). The relative stability analysis also shows that the relative intensity ratio 756/416 performs better than the other peaks identified, as shown in Fig. 11. Therefore, the most intense Raman peaks for the two phases with the Raman band at 756 cm^{-1} for C3A and MA at 416 cm^{-1} seems to be the most promising and suitable for the quantitative estimation for binary samples of C3A–MA. **Figure 12** illustrates a linear regression constructed between the relative intensity and phase fraction for C3A. The R^2 value in Fig. 12 shows a very good value (R^2 = 0.98) however, a slight deviation from linear behaviour, especially for the high phase fraction region was observed.

3.2.3. CA–MA Samples

The results from Table 7 show that the relative intensity ratio of 524 for CA cm^{-1} and 416 cm^{-1} for MA had the highest linear regression coefficient of determination and mean absolute error compared to the other peak ratios in Table 7. Additionally, Fig. 13 demonstrates that the relative intensity ratio of 522/416 performed better in the relative stabilities estimation. **Figure 14** shows a calibration curve between the 522/416 ratio and measured phase fractions for CA in the CA–MA samples, Therefore, for samples containing CA and MA, the relative intensity ratio of 522/416 was found to be the most suitable for a phase content analysis since it also shows the most intense peaks for these phases. The most suitable intensity ratio candidate did not have the highest R^2 value of 1, which could be attributed to some scattering in the sample content reaching about 50 wt% for the CA and MA content as illustrated in Fig. 14.

3.2.4. Al_2O_3–MA Samples

Table 8 shows the analysis conducted for samples that consist of Al_2O_3–MA, demonstrating the ratio of intensities of the Raman shifts at 773 cm^{-1} for MA and the Raman shift at 648 cm^{-1} for Al_2O_3 had the best coefficient of determination values with the lowest mean absolute error (MAE) compared to the other peaks ratios for these phases. Additionally, Fig. 15 shows that these medium peaks had better relative stabilities compared to the most intense peaks for the binary sample of Al_2O_3–MA. The most intense Raman shift of 416 for MA and 424 for Al_2O_3 are quite close to each other, therefore there is potential for the peak to overlap, which could affect the intensity of the peak measured. It could be concluded that intensities at shifts 648 cm^{-1} and 773 cm^{-1} were the most suitable relative intensities for the prediction of the phase content of MA or Al_2O_3, in the MA–Al_2O_3 binary system. **Figure 16** illustrates a linear correlation between the ratio of 648 cm^{-1} for Al_2O_3 and 773 cm^{-1} MA and the phase content (wt%) for Al_2O_3.

In Fig. 16, some slight deviation from the linear behaviour is observed around 50 wt% content for the phases (MA and Al_2O_3) and where there was a high phase difference. This could be associated with the use of medium intensity Raman peaks for the analysis. The most intense peaks could not be used because of peak overlap, which may contribute to not achieving the highest R^2 value.

3.2.5. Potential Source of Error in the Measurements

The calibration curves constructed between the relative intensities and phase fractions, as shown in Figs. 12, 14 and 16 had a slight deviation from the linear correlation (R^2 values 0.98, 0.97 and 0.96), and this was observed in the regions for samples with a high phase fraction difference. An instrumental variation could account for this phenomenon. Vibrational spectroscopy such as Raman spectroscopy could pose some challenges such as possible varying incident laser power and the response-ability of the detection system and this could cause a shift in the position of the Raman peaks.

3.3. Analysis of Non-stoichiometric Phases

The study also examined a possible variation in the peak position for the spinel material used as a reference by introducing an excess amount of MgO and Al_2O_3. The excess amount was varied in weight percentages of 2, 5 and 10 wt% and added to the reference spinel samples, as shown in Table 4. The non-stoichiometric region of interest was between 20 ± 0.5 and 50.5 ± 0.5 percentage weight (wt%) for MgO under 1 600°C in the Al_2O_3–MgO system using a slag atlas.[43] **Figures 17** and **18** show the Raman spectra for the reference spinel and the addition of an excess amount of MgO or Al_2O_3. The Raman peak for the most intense peak at 416 cm^{-1} in Figs. 17 and 18 varied within the range of ± 3 cm^{-1} when compared to the reference spinel. **Table 9** shows the Raman spectra measured from these samples with different contents of MgO and Al_2O_3. In Table 9, an estimation of the intensity ratio between the most intense peak and medium peaks for the reference spinel and those doped with the addition of MgO or Al_2O_3 was calculated by using Eq. (1) as presented in section 2.4. The peak ratios calculated were used to determine the difference between the reference spinel and the ones with excess MgO or Al_2O_3.

The evaluation values are shown in Table 9. The positioning of the Raman spectra in **Figs.** 18 and **19** shows only a slight variation in the reference spinel composition as a result of the introduction of excess MgO or Al_2O_3 and does not significantly change the Raman shift band characteristic of $MgO.Al_2O_3$ spinel. Therefore, it could be concluded that an excess amount of ≤ 5 wt% for MgO or Al_2O_3 will not adversely affect the quantitative analysis.

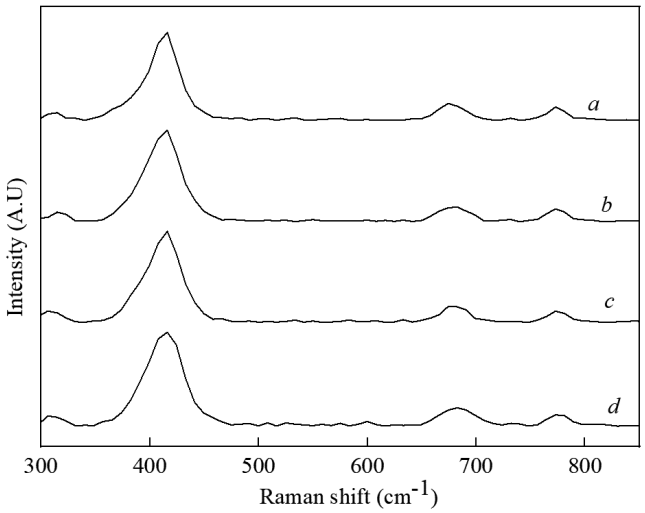

Fig. 17. Raman spectra for an excess amount of Al_2O_3 added to reference spinel. Where a) reference spinel, b) 2% excess amount of Al_2O_3, c) 5% excess amount of Al_2O_3 and d) 10% excess amount of Al_2O_3.

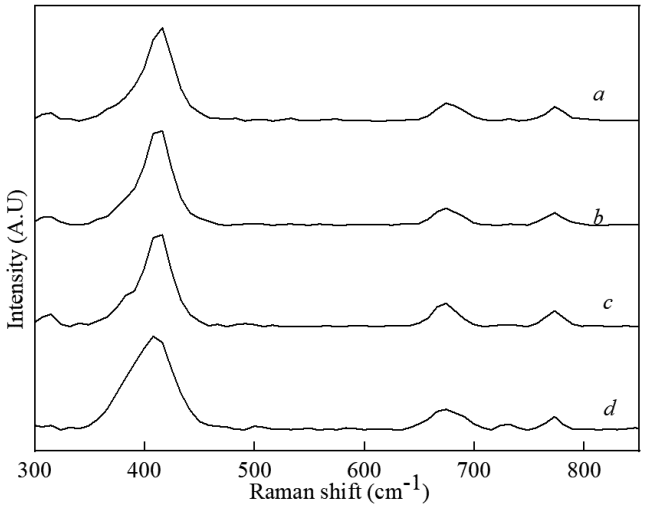

Fig. 18. Raman spectra for an excess amount of MgO added to the reference spinel. Where a) reference spinel, b) 2% excess amount of MgO, c) 5% excess amount of MgO and d) 10% excess amount of MgO.

3.4. Potential Practical Application

Spinel inclusions studied by other researchers[9–11] show that inclusions could be transformed into a mixture of $MgO–Al_2O_3–CaO$ inclusions, with an increasing calcium aluminate phase content due to calcium treatment. Figure 19 is a simplified schematic diagram that shows the modification process, and depending on the progress of the evolution process, two or more phases could be formed. The authors have previously[40] demonstrated the applicability of Raman spectroscopy to quantify calcium aluminate inclusions of C12A7, CA and C3A around the liquidus region. This current work illustrates the use of Raman spectroscopy to identify and to quantify the synthesised composition of $MgO.Al_2O_3–(CaO)_x(Al_2O_3)_y$.

Therefore, the application of Raman spectroscopy as a characterisation technique for oxide inclusions that consist

Table 9. Raman peaks for the excess amount of Al_2O_3 and MgO added to reference spinel samples.

Excess addition of Al_2O_3 and MgO (wt%)		Measured peaks [Raman shift (cm^{-1})]			Raman peaks ratios	
		Intense peak	Medium peak	medium peak	416/674 (682)	416/773
MA (reference spinel)		416	674	773	0.84	0.87
Al_2O_3	2	416	682	773	0.84	0.88
	5	416	682	773	0.80	0.89
	10	416	674	773	0.82	0.89
MgO	2	416	674	773	0.85	0.88
	5	416	674	773	0.80	0.85
	10	418	674	773	0.84	0.88

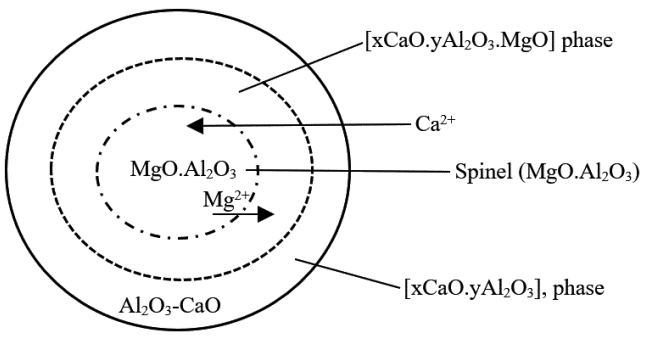

Fig. 19. Schematic modification of an $MgO·Al_2O_3$ inclusion with calcium into $CaO–Al_2O_3–MgO$ inclusion.[44–46]

of a mixture of spinel and calcium aluminates phases provides a practical opportunity to identify the inclusion type and estimate their phase composition. Primarily this could be used for the study of laboratory and industrial steel samples that may consist of multiphase inclusions since the use of Raman spectroscopy requires less sample preparation compared to conventional inclusion characterisation techniques.

The work illustrates the use of Raman spectroscopy for the characterisation of binary mixtures that contain spinel, aluminium oxide and calcium aluminates phases of CA, C3A and C12A7. However, industrial steel samples may contain more oxide or sulphide phases that are generated in the process of modifying or controlling the spinel inclusions. In future studies, a multiphase analysis of three or more phases could be conducted using Raman spectroscopy.

4. Conclusion

This study demonstrates the potential application of using Raman spectroscopy as an analytical technique for qualitative and quantitative analysis to estimate the phase fractions for a mixture of spinel and calcium aluminate phases. This study provides a technique for quantifying spinel and calcium aluminate inclusions in steel samples.

The findings of this work can be summarised as follows:

- The Raman shift for the calcium aluminate phases of CA at 524 cm^{-1}, C3A at 756 cm^{-1} and C12A7 at 517 cm^{-1} and for the MA at 416 cm^{-1} were found to be the most suitable for quantifying binary samples of CA–MA, C3A–MA and C12A7–MA. For an A–MA binary sample, the Raman bands at 648 cm^{-1} for Al_2O_3 and 773 cm^{-1} for MA were identified as the most suitable for the prediction of the phase composition.
- The Raman spectra measured from a non-stoichiometric spinel solid solution prepared at 1 600°C recorded a shift within the scope of ± 3 cm^{-1} from the reference spinel for the most intense Raman band.
- A potential practical application of Raman spectroscopy could be the identification of magnesium-aluminate spinel transformations in a mixture of $MgO–Al_2O_3–CaO$ phases in industrial scale steelmaking.

Acknowledgement

The authors wish to acknowledge the support of I4Future doctoral programme funded by European Union's H2020 under the Marie Skłodowska-Curie grant agreement No 713606 and Academy of Finland Profilation project (Academy of Finland, No. 311934).

REFERENCES

1) E. I. Castro-Cedeño, M. Herrera-Trejo, M. Castro-Román, F. Castro-Uresti and M. López-Cornejo: *Metall. Mater. Trans. B*, **47** (2016), 1613.
2) F. Tehovnik, J. Burja, B. Arh and M. Knap: *Metalurgija*, **54** (2015), 371.
3) Z. Y. Xu, J. H. Liu, Z. J. He and Q. H. Pang: *Metalurgija*, **57** (2018), 79.
4) Z. Deng, M. Zhu and D. Sichen: *Metall. Mater. Trans. B*, **47** (2016), 3158.
5) J. Poirier: *Metall. Res. Technol.*, **112** (2015), 410.
6) G. Okuyama, K. Yamaguchi, S. Takeuchi and K. Sorimachi: *ISIJ Int.*, **40** (2000), 121.
7) Y. Sun, Y. Zeng, R. Xu and K. Cai: *Int. J. Miner. Metall. Mater.*, **21** (2014), 1068.
8) L. Kong, Z. Deng and M. Zhu: *ISIJ Int.*, **57** (2017), 1537.
9) S. F. Yang, J. S. Li, Z. F. Wang, J. Li and L. Lin: *Int. J. Miner. Metall. Mater.*, **18** (2011), 18.
10) N. Verma, P. C. Pistorius, R. J. Fruehan, M. S. Potter, H. G. Oltmann and E. B. Pretorius: *Metall. Mater. Trans. B*, **43** (2012), 830.
11) C. W. Seo, S. H. Kim, S. K. Jo, M. O. Suk and S. M. Byun: *Metall. Mater. Trans. B*, **41** (2010), 790.
12) P. C. Pistorius, P. Presoly and K. G. Tshilombo: Sohn Int. Symp. on Advanced Processing of Metals and Materials: Principles, Technologies and Industrial Practice, TMS, Warrendale, PA, (2006), 373.
13) E. B. Pretorius, H. G. Oltmann and T. Cash: *Iron Steel Technol.*, **7** (2010), 31.
14) B. H. Reis, W. V. Bielefeldt and A. C. F. Vilela: *ISIJ Int.*, **54** (2014), 1584.
15) B. H. Reis, W. V. Bielefeldt and A. C. F. Vilela: *J. Mater. Res. Technol.*, **3** (2014), 179.
16) J. H. Park and H. Todoroki: *ISIJ Int.*, **50** (2010), 1333.
17) S. Imashuku, K. Ono, R. Shishido, S. Suzuki and K. Wagatsuma: *Mater. Charact.*, **131** (2017), 210.
18) S. Imashuku and K. Wagatsuma: *Metall. Mater. Trans. B*, **49** (2018), 2868.
19) S. Abdelaziz, G. Megahed, I. El-Mahallawi and H. Ahmed: *Ironmaking Steelmaking*, **36** (2009), 432.
20) B. G. Bartosiaki, J. A. M. Pereira, W. V. Bielefeldt and A. C. F. Vilela: *J. Mater. Res. Technol.*, **4** (2015), 235.
21) J. R. Ferraro, K. Nakamoto and C. W. Brown: Introductory Raman Spectroscopy, 2nd ed., Elsevier, Cambridge, (2003), 15.
22) R. Loudon: *Adv. Phys.*, **50** (2001), 813.
23) H. G. M. Edwards: Modern Raman Spectroscopy—A Practical Approach, John Wiley and Sons, Chichester, (2005), 210.
24) N. Noguchi, K. Shinoda and K. Masuda: *J. Mineral. Petrol. Sci.*, **104** (2009), 253.
25) A. Dandeu, B. Humbert, C. Carteret, H. Muhr, E. Plasari and J. M. Bossoutrot: *Chem. Eng. Technol.*, **29** (2006), 221.
26) J. B. Kimbrell, C. M. Crittenden, W. J. Steward, F. A. Khan, A. C. Gaquere-Parker and D. A. Stuart: *Nanosci. Methods*, **3** (2014), 40.
27) M. P. O'Horo, A. L. Frisillo and W. B. White: *J. Phys. Chem. Solids*, **34** (1973), 23.
28) H. Cynn, S. K. Sharma, T. F. Cooney and M. Nicol: *Phys. Rev. B*, **45** (1992), 1.
29) S. Dash, R. K. Sahoo, A. Das, S. Bajpai, D. Debasish and S. K. Singh: *J. Alloys Compd.*, **726** (2017), 1186.
30) A. Chopelas and A. M. Hofmeister: *Phys. Chem. Miner.*, **18** (1991), 279.
31) H. Cynn, O. L. Anderson and M. Nicol: *Pure Appl. Geophys.*, **141** (1993), 415.
32) L. M. Fraas, J. E. Moore and J. B. Salzberg: *J. Chem. Phys.*, **58** (1973), 3585.
33) M. Ruszak, S. Witkowski, P. Pietrzyk, A. Kotarba and Z. Sojka: *Funct. Mater. Lett.*, **4** (2011), 183.
34) D. R. Neuville, G. S. Henderson, L. Cormier and D. Massiot: *Am. Mineral.*, **95** (2010), 1580.
35) E. Feizi, J. J. Ojeda and A. K. Ray: *J. Mater. Sci. Mater. Electron.*, **25** (2014), 2261.
36) D. Torréns-Martín, L. Fernández-Carrasco, S. Martínez-Ramírez, J. Ibáñez, L. Artús and T. Matschei: *J. Am. Ceram. Soc.*, **96** (2013), 3589.
37) S. Li and L. H. Hihara: *J. Raman Spectrosc.*, **48** (2017), 137.
38) K. Baumann and N. Stiefl: *J. Comput. Aided Mol. Des.*, **18** (2004), 549.
39) K. Baumann: *Trends Anal. Chem.*, **22** (2003), 395.
40) F. Gyakwaa, M. Aula, T. Alatarvas, T. Vuolio, M. Huttula and T. Fabritius: *ISIJ Int.*, **59** (2019), 1846.
41) J. Thapa, B. Liu, S. D. Woodruff, B. T. Chorpening and M. P. Buric: *Appl. Opt.*, **56** (2017), 8598.
42) A. Misra, H. D. Bist, M. S. Navati, R. K. Thareja and J. Narayan: *Mater. Sci. Eng. B*, **79** (2001), 49.
43) M. Kowalski, P. J. Spencer and D. Neuschitz: Slag Atlas, Verein Deutscher Eisenhuttenleute, Verlag Stahleisen Gmbh, Düsseldorf, (1995), 64.
44) S. Yang, Q. Wang, L. Zhang, J. Li and K. Peaslee: *Metall. Mater. Trans. B*, **43** (2012), 731.
45) H. Y. Tang, Y. Wang, T. Wu, J. S. Li and S. F. Yang: *Ironmaking Steelmaking*, **44** (2017), 377.
46) M. Jiang, X. Wang, B. Chen and W. Wang: *ISIJ Int.*, **50** (2010), 95.